

# Numerical Simulations on Hypersonic Shock Wave/Boundary Layer Interactions by a Third-order Optimized Symmetric WENO Scheme

LI Chen<sup>1,2</sup>, GUO Qilong<sup>1,2</sup>, LI Qin<sup>1,2\*</sup>, ZHANG Hanxin<sup>1,2</sup>

1. State Key Laboratory of Aerodynamics, China Aerodynamics Research and Development Center, Mianyang 621000, P. R. China;
2. Computational Aerodynamics Institute, China Aerodynamics Research and Development Center, Mianyang 621000, P. R. China

(Received XX X Month 2016; revised XX X Month 2016; accepted XX X Month 2016)

**Abstract:** In this paper, a new third-order optimized symmetric weighted essentially non-oscillatory (WENO-OS3) scheme is used to simulate the hypersonic shock wave/boundary layer interactions. Firstly, the scheme is presented with the achievement of low dissipation in smooth region and robust shock-capturing capabilities in discontinuities. The Maxwell slip boundary conditions are employed to consider the rarefied effect near the surface. Next, several validating tests are given to show the good resolution of the WENO-OS3 scheme and the feasibility of the Maxwell slip boundary conditions. Finally, hypersonic flows around the hollow cylinder truncated flare and the 25°/55° sharp double cone are studied. Discussions are made on the characteristics of the hypersonic shock wave/boundary layer interactions with and without the consideration of the slip effect. The results indicate that the scheme has a good capability on predicting heat transfer and a high resolution on describing fluid structures. With the slip boundary conditions, the separation region at the corner is smaller and the prediction is more accurate than that with no-slip boundary conditions.

**Key words:** hypersonic flows; shock wave/boundary layer interactions; WENO scheme; slip boundary conditions

**CLC number:** V211.3

**Document code:** A

**Article ID:** XXXX-1120(201X)03-0219-21

## 0 Introduction

Hypersonic viscous flow interactions between shock wave and boundary layer have been studied by both numerical simulations and experimental measurements<sup>[1]</sup>. The interactions could cause the formation of a separation region and lead to an increase of heat transfer on the wall near the reattachment point. These effects are necessary to the control and thermal protection of hypersonic vehicles. Recently, the NATO Research Technology Organization (RTO) has fostered a series of studies on hypersonic flow interactions. Two configurations chosen for the studies were the hollow cylinder fare and the sharp double cone, and the current numerical simulations mainly focus on the laminar flows.

Numerical simulations on these problems are performed by at least two types of approaches nowadays.

One type is the kinetic approach including DSMC method and some approaches based on the Boltzmann equations. The other type is the continuum approach, such as the traditional computational fluid dynamic (CFD) method using Navier-Stokes (NS) equations. The DSMC method is appropriate for all flow regimes, while the CPU time cost (especially when the Knudsen number is less than 0.001) is huge relatively. Usually solving the NS equations is about an order of magnitude faster than the DSMC method<sup>[2]</sup>. However, the NS equations are invalid in rarefied flow regimes because they are based on the continuum assumption. Therefore, it is attractive to find ways to extend the validity of the NS solver beyond the continuum regime.

Researchers found that the traditional CFD modeling in near continuum regime or slip regime can be improved by using the slip boundary conditions. The most common-used slip boundary conditions are

\*Corresponding author: Li Qin, Professor, E-mail: qin-li@vip.tom.com.

**How to Cite this article:** Li chen, Guo qilong, Li qin, et al. Numerical simulations on hypersonic shock wave/boundary layer interactions by a third-order optimized symmetric WENO scheme[J]. Trans. Nanjing Univ. Aeronaut. Astronaut., 201X,XX(X):219-239.

<http://dx.doi.org/10.16356/j.1005-1120.2014.03.219>

Maxwell<sup>[3]</sup> slip velocity and Smoluchowski<sup>[4]</sup> temperature jump boundary conditions. Gökçen and MacCormack<sup>[5, 6]</sup> proposed more general boundary conditions and extended them to larger Knudsen numbers. To correct the linear variability of shear stress near the wall, a wall function approach for boundary condition was proposed by Lockerby et al<sup>[7]</sup>. Several second order slip boundary conditions<sup>[8-11]</sup> have also been developed to extend the validity of NS solver. However, it was reported<sup>[12]</sup> that the second order slip boundary conditions did not appear to work better than the first order ones in hypersonic flow simulations.

For NS solver, developing numerical schemes for shock-capturing is important in hypersonic computation. Nowadays, the TVD schemes, such as the non-oscillatory, non-free-parameter and dissipation (NND) scheme<sup>[13]</sup>, are the most widely used in the design phase of hypersonic vehicles. Due to the increasing requirement of accurate prediction on aerodynamics and aerothermodynamics, the weighted essentially non-oscillatory (WENO) scheme proposed by Liu et al.<sup>[14]</sup> and extended by Jiang and Shu<sup>[15]</sup> has gained more attentions in recent years<sup>[16]</sup>. Moreover, some high order compact schemes are used in the supersonic/hypersonic flows simulation<sup>[17, 18]</sup>. High order schemes usually need more nodes compared with NND scheme when constructing the flux vectors. For example, it needs seven nodes in the fifth order WENO scheme, which would cause overshoot in the vicinity of shock wave, have difficulty in simulating the flows around complex geometries, and is not easy to extend it to the multi-block computational code due to the high order interface boundary condition. Therefore, a five nodes scheme, which has high accurate resolution and the number of nodes is the same as NND scheme, is studied here. It cost little to modify from the existing NND codes, and the new third order scheme aims at engineering computation.

In this paper, a new optimized symmetric third-order weighted essentially non-oscillatory (WENO-OS3) scheme is used to simulate hypersonic shock wave/boundary layer interactions. The WENO-OS3 scheme and slip boundary conditions are described in Section 2. The validations of the numerical methods are presented in section 3. In Section 4, Mach 9.91 flow around a hollow cylinder flare and Mach 15.6

flow around a 25° sharp double cone are simulated and discussed. Conclusions are given in the last section.

## 1 Numerical Methods

### 1.1 Governing equations

In the generalized computational coordinates, the dimensionless time-dependent compressible NS equations can be expressed in the conservative form as follows:

$$\frac{\partial \hat{Q}}{\partial t} + \frac{\partial \hat{E}}{\partial \xi} + \frac{\partial \hat{F}}{\partial \eta} + \frac{\partial \hat{G}}{\partial \zeta} = \frac{\partial \hat{E}_v}{\partial \xi} + \frac{\partial \hat{F}_v}{\partial \eta} + \frac{\partial \hat{G}_v}{\partial \zeta}, \quad (1)$$

where

$$\hat{Q} = J^{-1}Q,$$

$$\hat{E} = J^{-1}(\xi_x E + \xi_y F + \xi_z G),$$

$$\hat{F} = J^{-1}(\eta_x E + \eta_y F + \eta_z G),$$

$$\hat{G} = J^{-1}(\zeta_x E + \zeta_y F + \zeta_z G),$$

$$\hat{E}_v = J^{-1}(\xi_x E_v + \xi_y F_v + \xi_z G_v),$$

$$\hat{F}_v = J^{-1}(\eta_x E_v + \eta_y F_v + \eta_z G_v),$$

$$\hat{G}_v = J^{-1}(\zeta_x E_v + \zeta_y F_v + \zeta_z G_v),$$

$$Q = [\rho \quad \rho u \quad \rho v \quad \rho w \quad e]^T,$$

$$E = \begin{bmatrix} \rho u \\ \rho u^2 + p \\ \rho uv \\ \rho uw \\ (e+p)u \end{bmatrix}, \quad F = \begin{bmatrix} \rho v \\ \rho vu \\ \rho v^2 + p \\ \rho vw \\ (e+p)v \end{bmatrix},$$

$$G = \begin{bmatrix} \rho w \\ \rho wu \\ \rho wv \\ \rho w^2 + p \\ (e+p)w \end{bmatrix}, \quad E_v = \frac{1}{\text{Re}} \begin{bmatrix} 0 \\ \tau_{xx} \\ \tau_{xy} \\ \tau_{xz} \\ b_x \end{bmatrix},$$

$$F_v = \frac{1}{\text{Re}} \begin{bmatrix} 0 \\ \tau_{yx} \\ \tau_{yy} \\ \tau_{yz} \\ b_y \end{bmatrix}, \quad G_v = \frac{1}{\text{Re}} \begin{bmatrix} 0 \\ \tau_{zx} \\ \tau_{zy} \\ \tau_{zz} \\ b_z \end{bmatrix},$$

$$e = \rho[C_v T + \frac{1}{2}(u^2 + v^2 + w^2)],$$

$$b_i = u\tau_{ix} + v\tau_{iy} + w\tau_{iz} + q_i,$$

$$\tau_{ij} = \mu \left( \frac{\partial u_i}{\partial x_j} + \frac{\partial u_j}{\partial x_i} - \frac{2}{3} \delta_{ij} \frac{\partial u_k}{\partial x_k} \right),$$

$$q_i = -\frac{\mu}{(\gamma-1)Ma^2 \text{Pr}} \frac{\partial T}{\partial x_i}.$$

In the above equations,  $J$  is the transformation Jacobian,  $\xi_x, \xi_y, \xi_z$  are grid metrics,  $Q$  is the vector of conservative variables,  $E, F, G$  are inviscid fluxes,  $Ev, Fv, Gv$  are viscous fluxes,  $u, v, w$  are the Cartesian velocity components in  $x, y, z$  directions,  $\rho$  is density,  $p$  is static pressure,  $T$  is temperature,  $C_v$  is the specific heat at constant volume,  $e$  is total energy,  $\tau$  is stress tensor,  $\mu$  is dynamic viscosity,  $q$  is heat transfer vector,  $Re$  is the Reynolds number,  $Pr$  is the Prandtl number, and  $\gamma$  is specific heat ratio.

## 1.2 WENO-OS3 scheme

An optimized symmetric third-order scheme optimized from Ref. [19] for inviscid flux term discretization is introduced. The one-dimensional scalar conservation law is used for investigation:

$$u_t + f(u)_x = 0. \quad (2)$$

With the domain discretized into uniform intervals of  $\Delta x$ , the semi-discretized conservative scheme can be written as:

$$(u_t)_j = -(\hat{f}_{j+1/2} - \hat{f}_{j-1/2})/\Delta x, \quad (3)$$

where  $\hat{f}_{j+1/2}$  approximates  $h_{j+1/2} = h(x_{j+1/2})$  to a high order with  $h(u)$  implicitly defined by

$$f(u(x)) = \frac{1}{\Delta x} \int_{x-\Delta x/2}^{x+\Delta x/2} h(\xi) d\xi. \quad (4)$$

When applied in computation,  $f(u)$  is usually split into two parts:

$$f(u) = f^+(u) + f^-(u). \quad (5)$$

In this paper, the Steger-Warming flux vector splitting is used. Then the numerical fluxes are obtained from the positive and negative parts of  $f(u)$ , namely:

$$\hat{f}_{j+1/2} = \hat{f}_{j+1/2}^+ + \hat{f}_{j+1/2}^-, \quad (6)$$

where the  $\hat{f}_{j+1/2}^+$  and  $\hat{f}_{j+1/2}^-$  are computed by WENO-OS3 scheme. We only describe the positive part of the numerical fluxes ( $\hat{f}_{j+1/2}^+$ ) here. For simplicity, the superscript "+" is omitted. The negative part of  $\hat{f}_{j+1/2}$  is symmetric with respect to  $x_{j+1/2}$ .

### a. Linear part

In the optimized scheme, an additional candidate stencil is added downwind to the third-order WENO (WENO3) scheme. The numerical fluxes are obtained as:

$$\hat{f}_{j+1/2} = \alpha_0 \hat{f}_{j+1/2}^{(0)} + \alpha_1 \hat{f}_{j+1/2}^{(1)} + \alpha_2 \hat{f}_{j+1/2}^{(2)}, \quad (7)$$

where the  $\hat{f}_{j+1/2}^{(i)}$  is the approximation of the flux  $h_{j+1/2}$  on  $i^{\text{th}}$  candidate stencil. The forms of  $\hat{f}_{j+1/2}^{(i)}$  are

$$\begin{aligned} \hat{f}_{j+1/2}^{+(0)} &= f_j^+ + \frac{1}{2} \Delta f_{j-1/2}^+, \\ \hat{f}_{j+1/2}^{+(1)} &= f_j^+ + \frac{1}{2} \Delta f_{j+1/2}^+, \\ \hat{f}_{j+1/2}^{+(2)} &= f_{j+1}^+ - \frac{1}{2} \Delta f_{j+3/2}^+, \end{aligned} \quad (8)$$

where  $\Delta f_{j+1/2} = f_{j+1} - f_j$ ,  $a_i$  are the ideal weights of the scheme given by  $\alpha_0 = \frac{1}{3} - \alpha_2, \alpha_1 = \frac{2}{3}$ . After Fourier analysis, we obtain

$$\begin{aligned} \Re[\kappa'(\kappa)] &= \frac{1}{6}(-\sin 2\kappa + 8\sin \kappa), \\ \Im[\kappa'(\kappa)] &= \frac{1}{2}[-\beta \cos 2\kappa + 4\beta \cos \kappa - 3\beta], \end{aligned} \quad (9)$$

where  $\beta = 1/3 - 2\alpha_2$ ,  $\kappa$  is wavenumber, and  $\kappa'$  is modified wavenumber.  $\Re$  and  $\Im$  refer to the real and imaginary part of a complex number respectively. Because there is one free parameter for a third-order scheme in Eq. (7), the parameter  $n_{3rd}$  is introduced to adjust the dissipation level of the scheme. It is suggested that  $\Im[\kappa'(\pi)_{\text{WENO-OS3}}] = \frac{1}{n_{3rd}} \Im[\kappa'(\pi)_{\text{WENO3}}]$ , then  $\alpha_2 = (n_{3rd} - 1)/6n_{3rd}$ . The scheme turns out to be the WENO3 scheme for  $n_{3rd} = 1.0$ , and it becomes the fourth-order center difference scheme when  $n_{3rd} \rightarrow \infty$ . The bigger the  $n_{3rd}$  is, the lower the dissipation of WENO-OS3 will be. In this paper,  $n_{3rd} = 10$  is chosen.

### b. Nonlinear part

In order to capture the shock wave and discontinuity, the nonlinear technique should be used. The method used in WENO scheme is employed here, whose idea is to maximize the weight of the smooth candidate stencil while minimize the weight of the discontinuous stencil.

$$\begin{aligned} \hat{f}_{j+1/2} &= \sum_{i=0}^2 \omega_i \hat{f}_{j+1/2}^{(i)}, \\ \omega_i &= \frac{\Omega_i}{\sum_{k=0}^2 \Omega_k}, \Omega_i = \frac{\alpha_i}{(\varepsilon + IS_i)^p}, \end{aligned} \quad (10)$$

where the  $IS_i$  is smoothness measurement on  $i^{\text{th}}$  candidate stencil given by  $IS_i = (f_{j+i} - f_{j-i})^2$ . In the smooth regions, the nonlinear weights are approximately equal to the ideal weights.

Considering the stability of the scheme while decreasing the dissipation error further, the nonlinear weights should be close to the ideal weights as much as possible<sup>[15]</sup>. To reach this goal, a method with variation

of the power in the Eq. (10) was proposed by Li et al<sup>[19]</sup>. The algorithm is given as follows:

$$\begin{aligned} p &= \max(p_1, p_2), \\ p_1 &= TF\left(\left|\Delta f^+\right|_{\max}; 8, p_{1l}, p_{1u}\right), \\ p_2 &= TF\left(r_{\left|\Delta f^+\right|_{\max}}; 8, p_{2l}, p_{2u}\right), \\ \left|\Delta f^+\right|_{\max} &= \text{rescale}(\max_{i=0..2} \left|\sqrt{IS_i}\right|), \\ r_{\left|\Delta f^+\right|_{\max}} &= \begin{cases} \frac{\max_{i=0..2} \sqrt{IS_i}}{\varepsilon + \min_{i=0..2} \sqrt{IS_i}} & \text{if } \left|\sqrt{IS_i}\right|_{\max} > r_u p_{1l}, \\ 1.0 & \text{else} \end{cases} \end{aligned} \quad (11)$$

where  $p_l$  and  $p_u$  are the powers computed by the transition function  $TF$ , which is given by

$$TF(x; c, x_l, x_u) = 1 + \tanh\left(\frac{c(x - [(x_u + x_l)/2])}{x_u - x_l}\right). \quad (12)$$

The constant  $c$  in Eq.(12) refers to the extent of the inclination.  $x_u$  and  $x_l$  are upper and lower thresholds respectively.  $TF$  value equals to 2 for  $x > x_u$ , and it equals to 0 for  $x < x_l$ . In order to avoid the parameters in the algorithm being problem-dependent, a specific *rescale* function was used when  $p_l$  is computed. The function is given as follows:

$$\begin{aligned} \text{rescale}(\bar{x}) &= \Phi_1 \Phi_2 \Phi_3 \bar{x}, \\ \Phi_1 &= 1 / \left( J^{-1} \sqrt{k_x^2 + k_y^2 + k_z^2} \right), \\ \Phi_2 &= L_{ref} L^{-1}, \Phi_3 = 1 / \sqrt{\rho_b (\rho u^2 + p)_b}, \end{aligned} \quad (13)$$

where  $\Phi_1$  is related to grid transformation.  $k_x$  refers to  $\xi_x$ ,  $\eta_x$ ,  $\zeta_x$  when it is discretized in  $x$ ,  $y$ ,  $z$  directions respectively. The definitions of  $k_y$  and  $k_z$  are similar to that of  $k_x$ .  $\Phi_2$  is related to the characteristic matrix used in the process of  $\hat{f}_{j+1/2}$  reconstruction.  $L$  is the left characteristic matrix you used, and  $L_{ref}$  is the reference one, they are both given in the appendix.  $\Phi_3$  is a factor related to different physical problems. The subscript “ $b$ ” denotes the reference state related to the boundary condition usually chosen as the inflow or the upstream state of a shock wave.

Finally the power is obtained by the maximum of the  $p_l$  and  $p_u$ . The parameters used in the scheme are calibrated to be:  $c=8$ ,  $p_{1l}=0.022$ ,  $p_{1u}=0.029$ ,  $p_{2l}=3.2$ ,  $p_{2u}=3.8$ .

A second-order central difference scheme is applied to the viscous fluxes, and the lower-upper symmetric Gauss-Seidel (LU-SGS) method for time approaching is

adopted. It is assumed that the gas is perfect gas for all cases in this paper, so  $\gamma$  is constant for calculation.

### 1.3 Slip boundary conditions

#### a. Maxwell boundary conditions

Using slip boundary conditions can extend the validity of the NS solver beyond the continuum regime. The Maxwell boundary condition is first derived for a flat plate<sup>[3]</sup>. It is given by:

$$\begin{aligned} u_s - u_w &= \frac{2-\sigma}{\sigma} \lambda \left( \frac{\partial u_\tau}{\partial n} + \frac{\partial u_n}{\partial \tau} \right)_{gw} \\ &+ \frac{3}{4} \frac{\mu}{\rho_{gw} T_{gw}} \left( \frac{\partial T}{\partial \tau} \right)_{gw}. \end{aligned} \quad (14)$$

where  $n$  and  $\tau$  are the direction normal and tangential to the wall respectively,  $u_s$  is the slip velocity,  $u_w$  is the wall velocity,  $\sigma$  is the momentum accommodation coefficient,  $u_\tau$  is the tangential velocity along the wall, the subscript “ $gw$ ” means the physical quantities of gas at the surface.  $\lambda$  refers to the mean free path calculated from local gas flow properties:

$$\lambda = \frac{2\mu}{\rho c} = \frac{2\mu}{\rho \sqrt{8RT/\pi}}, \quad (15)$$

Where  $\bar{c}$  is the mean molecular speed and  $R$  is the gas constant. For an isothermal wall, it is simplified as:

$$u_s - u_w = \frac{2-\sigma}{\sigma} \lambda \left( \frac{\partial u_\tau}{\partial n} \right)_{gw}, \quad (16)$$

The temperature jump boundary condition at the wall is given by:

$$T_s - T_w = \frac{2-\alpha}{\alpha} \frac{2\gamma}{(\gamma+1)\text{Pr}} \lambda \left( \frac{\partial T}{\partial n} \right)_{gw}, \quad (17)$$

where  $\alpha$  is thermal momentum accommodation coefficient.

#### b. Implementation of the Maxwell boundary conditions

Due to the impermeable wall boundary condition at the wall, the slip velocity only has the tangential component. The stationary body is considered with the wall velocity  $u_w$  as 0.0, and the results present are calculated assuming a fully diffuse wall, with a corresponding accommodation coefficient of 1.0. Then the velocity slip boundary condition Eq. (16) is simplified as:

$$\left( u_\tau - \lambda \frac{\partial u_\tau}{\partial n} \right)_{gw} = 0. \quad (18)$$

The temperature jump boundary condition at the wall can also be written as:

$$\left( T - \lambda_T \frac{\partial T}{\partial n} \right)_{\text{gw}} = T_w, \quad (19)$$

where  $\lambda_T = \frac{2\gamma}{(\gamma+1)\text{Pr}} \lambda$ .

A unified form of the Eq. (18) and (19) is given as follows:

$$\phi - a \nabla_n \phi = b. \quad (20)$$

where  $a$  refers to  $\lambda$  or  $\lambda_T$ , and  $b$  refers to zero or  $T_w$  respectively. It is obvious that the Eq. (20) is a Robin boundary condition, and it is discretized as follows:

$$\phi_s = \frac{bd + a\phi^1}{a + d}, \quad (21)$$

where  $d$  refer to the distance between the mesh along the wall and the first mesh away from wall. The superscript "1" refer to the quantity at the first mesh away from wall. The subscript "s" refers to the slip quantity at the surface. The Eq. (21) is the form of first-order difference, and it also could be discretized in a higher order form.

## 2 Validating Tests

In this section, validations of numerical methods are presented. Firstly, three cases are calculated to show the resolution of the WENO-OS3 scheme. i.e. Shu-Osher problem, flat plate shock wave / boundary layer interaction problem and RUN 28 sharp double cone problem. Next, two cases are simulated here to show the performances of the slip boundary conditions. One is the hypersonic flow over a flat plate, and the other is the hypersonic flows around a circular cylinder.

The non-dimensional coefficients referred to the results for describing the surface properties are defined as follows:

$$C_p = \frac{p - p_\infty}{\frac{1}{2} \rho_\infty u_\infty^2}, C_H = \frac{q}{\frac{1}{2} \rho_\infty u_\infty^3}, \quad (22)$$

$$St = \frac{q}{\rho_\infty u_\infty (H_0 - H_w)},$$

where the subscript " $\infty$ " refer to freestream parameter, and "w" means the physical quantities at the wall.  $C_p$  is

the pressure coefficients,  $C_H$  is the heat transfer coefficient,  $St$  is the Stanton number, and  $H$  represents the enthalpy.

A continuum breakdown parameter defined by Boyd et al [20] is used for visualizing the rarefied regions in the flow field here. The gradient-length local Knudsen number ( $Kn_{GLL}$ ) is given by:

$$Kn_{GLL} = \frac{\lambda}{Q} |\nabla Q|, \quad (23)$$

where  $Q$  is a physical quantity of interest such as pressure, temperature or density. The density is chosen in this paper. It is assumed that continuum breakdown occurs when  $Kn_{GLL}$  is greater than 0.05.

### 2.1 Shu-Osher problem

This test problem that a Mach 3 shock wave propagates into smooth density fluctuations was first proposed by Shu and Osher [21]. The test aims at accurately resolving the small scale structures behind the shock.

The initial conditions on the domain  $-4.5 \leq x \leq 4.5$  are as follows:  $u=0$ ,  $p=1$ , and  $\rho = 1 + 0.2 \sin(5x)$  for  $x \geq -4$ ;  $u=2.629369$ ,  $p=10.33333$ , and  $\rho = 3.857143$  for  $x < -4$ . The governing equations are one dimensional Euler equations simplified from Eq. (1). A third-order TVD Runge-Kutta method is used for temporal discretization in this case.

Solutions are obtained at  $t=1.8$ . Density fields on 800 mesh nodes from NND [13], WENO3 and WENO-OS3 schemes are shown in Fig. 1. The "exact" solution is obtained by the fifth-order WENO scheme on 1600 mesh nodes. In contrast, NND scheme yields excessively damped solutions, and the WENO3 solutions are less dissipative than that of NND. Similar results are found for WENO-OS3 scheme with better predictions of the wave amplitudes than the original WENO3 scheme. .

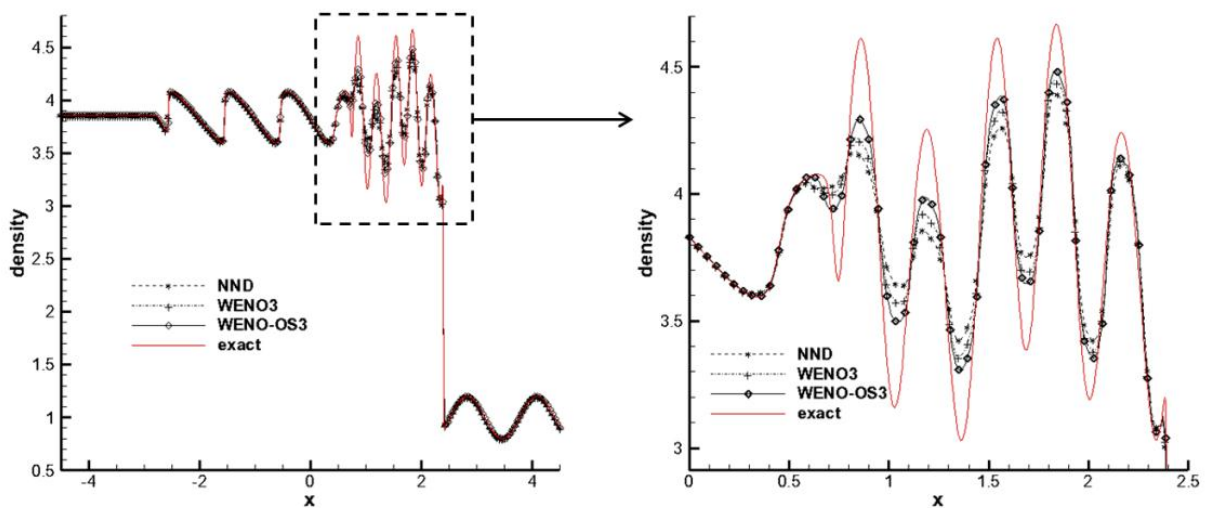


Fig. 1 Density fields at  $t=1.8$  on 800 mesh nodes

## 2.2 Flat plate shock wave/boundary layer interaction problem

This test problem, an external shock wave incident in a boundary layer on a flat plate, has become a benchmark of testing new numerical schemes since it first proposed in Ref [22].

The computational parameters are  $Ma_\infty = 2.0$ ,  $Re_\infty = 2.96 \times 10^5$ ,  $T_\infty = 293.0$ ,  $Pr = 0.72$ . The impinging shock angle is  $32.585^\circ$ . The computational domain is chosen to be  $0 \leq x \leq 2.02$ ,  $0 \leq y \leq 1.30$ . The number of mesh points used in this paper is  $103 \times 122$  in the streamwise and the normal directions, respectively. The adiabatic wall boundary condition is adopted.

Fig.2 presents the pressure contours and patterns of the separation bubble by different numerical schemes. It can be observed that the NND scheme does not capture the separation region with the same mesh, and the size of the bubble decreases with bigger dissipation of the scheme, i.e.  $L_{WENO5} > L_{WENO-OS3} > L_{WENO3} > L_{NND}$ .

## 2.3 Sharp double cone problem-RUN 28

Hypersonic flow of nitrogen around a  $25.755^\circ$  sharp

cone (SDC)<sup>[23]</sup> is calculated here. The number of mesh is  $266 \times 128$  in the streamwise and the normal directions, respectively.

The freestream conditions are  $Ma_\infty = 9.59$ ,  $T_\infty = 185.6K$ ,  $T_w = 293.3K$ ,  $Re_\infty = 1.39 \times 10^5 / m$ .

A laminar flow is ensured in this condition. The Sutherland law is used for modeling the dynamic viscosity.

The density gradient contours presented in Fig. 3 indicate that a train of reflected waves, which is generated between the layer formed by the slip line and the second cone surface, is resolved by the WENO-OS3 and WENO5 schemes. Two and three vortices are observed near the corner by WENO-OS3 and WENO5 schemes, respectively, while only one vortex captured by NND scheme. The Stanton number along the surface is given in Fig. 4, which shows that WENO-OS3 scheme is better than the NND scheme and worse than the WENO5 scheme on heat transfer prediction. Moreover, the heat flux distribution has a certain divergence from the experiment data due to the mesh is too coarse, and the results will be better with the mesh refinement.

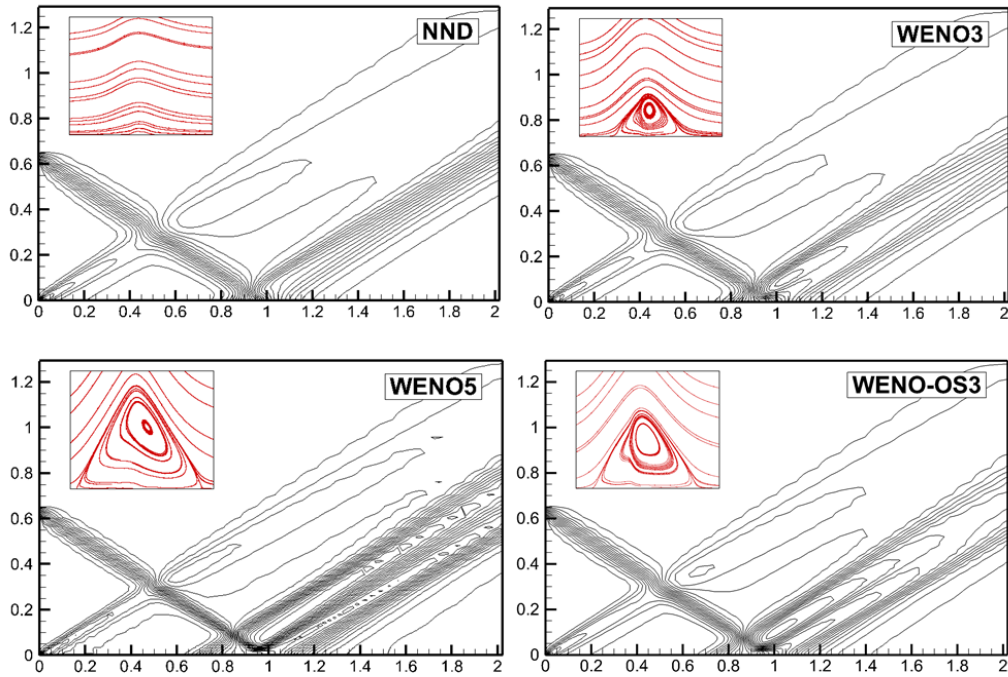


Fig. 2 Pressure contours and patterns of the separation bubble by different numerical schemes



Fig. 3 Density gradient contours and separation region by different numerical schemes

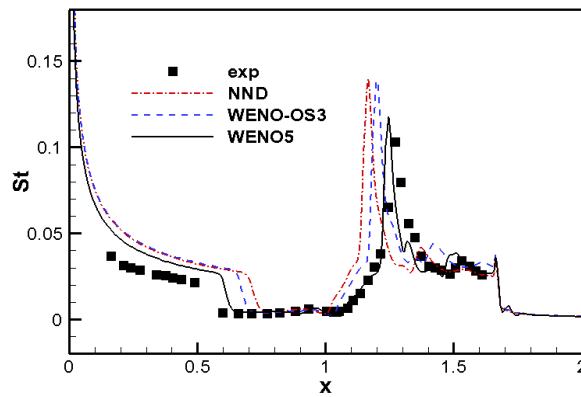


Fig. 4 Stanton number along the surface of 25°/55°SDC by different numerical schemes

## 2.4 Tests for the slip boundary conditions

Two cases computed by the WENO-OS3 scheme are tested here for validating the Maxwell slip boundary conditions. The results present here are calculated by assuming a fully diffuse wall with a corresponding accommodation coefficient of 1.

### a. Flat plate

Hypersonic flow of argon over a flat plate at  $0^\circ$  angle of attack which has a previous set of experiments [24] is considered here. The freestream parameters are  $T_\infty = 64.5K$ ,  $T_w = 292K$ ,  $p_\infty = 3.73Pa$ ,  $\lambda_\infty = 0.23mm$ ,  $Ma_\infty = 12.7$ . The Sutherland law is used for modeling the dynamic viscosity in this case, i.e.  $\mu = A_s T^{1.5} / (T + T_s)$ , where  $A_s = 1.93 \times 10^{-6} (Pa \cdot s K^{-1/2})$ , and  $T_s = 142K$ . The Prandtl number is 0.67, and  $\gamma$  is 1.67. The mesh of  $200 \times 140$  nodes in  $x$  and  $y$  directions is used in this study. The  $\Delta x = 0.15$  at  $x = 0mm$  and the  $\Delta y = 0.1$  at  $y = 0$  mm.

The Maxwell slip boundary conditions are employed at the wall. Fig.5 and 6 show the slip velocity and temperature jump along the flat plate. By comparison, the results of Maxwell slip boundary conditions agree well with that calculated by Nam et al [12].

### b. Circular cylinder

Hypersonic flows of argon over a circular cylinder

of radius  $d=304.8mm$  are studied here. Two inflow conditions of  $Kn_\infty=0.002$  and  $Kn_\infty=0.05$  are chosen from a series of typical cases in Ref [2]. The other free parameters can be found in Ref [2] in details. The power law model is used for viscosity. The number of mesh points used is  $100 \times 60$  in the streamwise and the normal directions, respectively.

Fig 7 presents the  $Kn_{GLL}$  fields for  $Kn_\infty=0.002$  and  $Kn_\infty=0.05$ . The results indicate that with the density decrease, the shock thickness increases, the shock standoff distance becomes longer, the rarefied effects becomes apparently.

Table 1 shows the peak heat transfer predicted by both no-slip and slip boundary conditions. It is clear that using the slip boundary conditions improves the agreement with the DSMC results from Ref. [2]. For  $Kn_\infty=0.002$  case, the peak heat transfer computed by all boundary conditions are in coincidence with the DSMC result. For  $Kn_\infty=0.05$  case, the no-slip result is over 10% difference diverge from the DSMC result, while it can be better predicted by using the slip boundary conditions. The heat transfer coefficient along the surface is shown in Fig. 8. All the CFD results are over predicted compared with the DSMC result. The no-slip CFD result shows larger difference from the DSMC result. It is greatly improved by using the Maxwell slip boundary conditions.

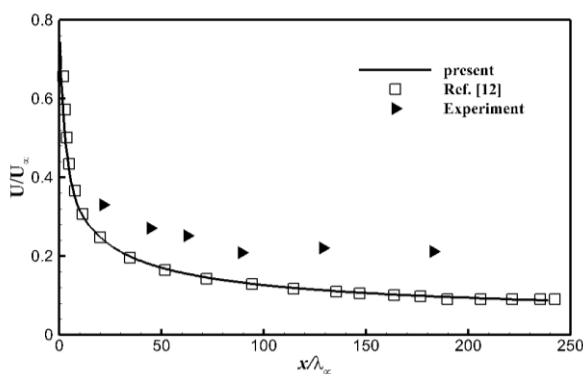


Fig. 5. The slip velocity along the flat plate surface

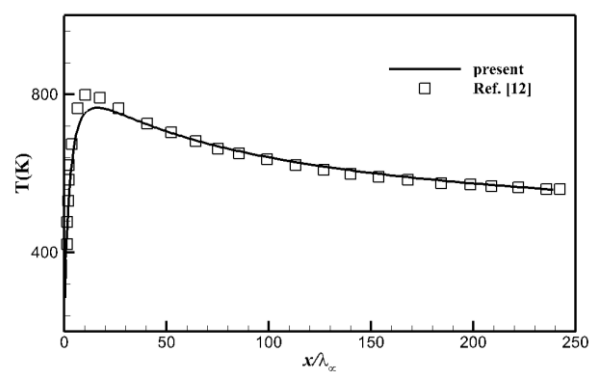
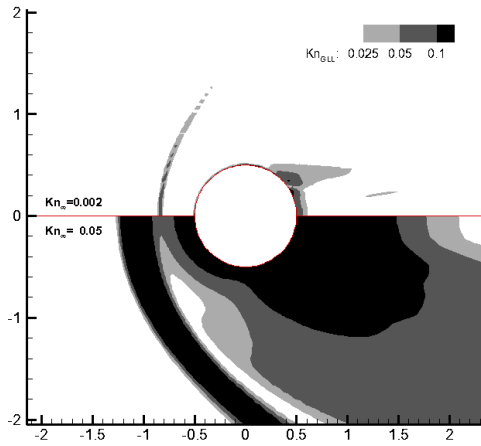
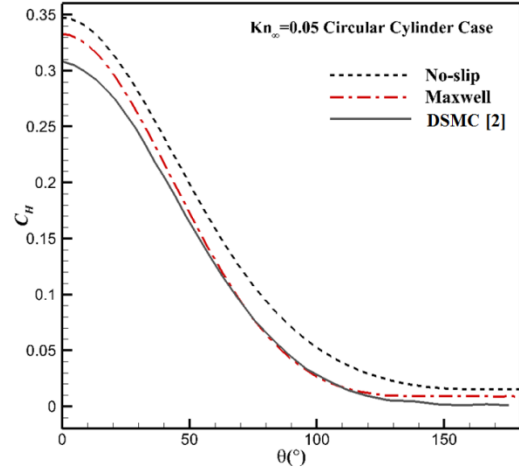


Fig. 6. The gas temperature along the flat plate surface

Fig. 7.  $Kn_{GLL}$  fields for  $Kn_\infty=0.002$  and  $Kn_\infty=0.05$ Fig. 8.  $Kn_\infty=0.05$  heat transfer coefficient distribution around the surfaceTable 1 Peak heat transfer ( $\text{kW/m}^2$ )

$Kn_\infty$	DSMC[2]	No-slip	Maxwell	No-slip[2]	Maxwell[2]
0.002	89.80	88.80(-1.11%)	90.29(0.44%)	89.84(0.06%)	89.14(-0.73%)
0.05	15.85	17.70(11.7%)	16.94(6.85%)	18.02(13.7%)	17.20(8.51%)

### 3 Investigations on Hypersonic Shock/Boundary Layer Interactions

In this section, the WENO-OS3 scheme is applied to investigate the hypersonic shock/boundary layer interactions in the flows around the hollow cylinder truncated flare and the  $25^\circ/55^\circ$  sharp double cone. Due to the axisymmetric geometry and the zero angle of attack, the axisymmetric NS equations are solved.

#### 3.1 Hollow cylinder truncated flare

Hypersonic flow of nitrogen around a hollow cylinder truncated flare (HCTF) which has a previous set of computational results<sup>[25-28]</sup> and experiments<sup>[25]</sup> is calculated here. The configuration and the computational mesh structure are shown in Fig. 9 and Fig. 10, respectively. The reference length is  $L=0.1017m$ .

The freestream parameters are  $T_\infty=51K$ ,  $T_w=293K$ ,  $p_\infty=6.3Pa$ ,  $Ma_\infty=9.91$ ,  $Re_\infty=1.86 \times 10^5/m$ , which ensure a laminar flow condition. The Sutherland law is used for modeling the dynamic viscosity in this case, i.e.  $\mu=A_s T^{1.5}/(T+T_s)$ , where  $A_s=1.4 \times$

$10^{-6}(\text{Pa}\cdot\text{sK}^{-1/2})$ , and  $T_s=106.7K$ . The specific heat ratio is  $\gamma=1.4$ , and the Prandtl number is  $Pr=0.71$ .

The parameters of the inlet flow and top boundary are set from the freestream. The zero gradient extrapolation method is used to the outflow boundaries. At the bottom boundary in front of the leading edge, the symmetric boundary condition is used.

##### a. Flow structures

Typical results of all cases are given in Table 2, where similar flow structures are obtained. Fig. 11 shows the pressure contours. The numerical schlieren picture and the streamlines at the corner for the HCTF case are presented in Fig. 12. A strong viscous interaction occurs at the leading edge of the HCTF, forming the laminar boundary. A recirculation zone is observed at the corner where it starts near  $x/L=0.7$  and reattaches near  $x/L=1.3$ . The leading edge shock wave, the separation shock wave and the reattachment shock wave interact with each other near the end of the conical part. The expansion waves are observed at the second corner.

##### b. Mesh convergence

To investigate the mesh convergence, three different meshes are conducted here, i.e. a coarse mesh ( $128 \times 128$ ), a medium mesh ( $256 \times 256$ ), and a fine mesh ( $512 \times 256$ ). The computations with those refer to CFD1, CFD2 and CFD3, respectively. Table 2 presents the positions of the separation points ( $X_s$ ) and reattachment points ( $X_R$ ) using different meshes and different wall boundary conditions. Good mesh convergence can be observed, and the recirculation region length increases with the mesh refinement. The converged results of NS equations are a little bigger than DSMC results<sup>[25]</sup> and experimental results<sup>[25]</sup>. The possible disagreement may be the influence of nonequilibrium effects, which is neglected when using the Eq. (1), and the inadequacy of slip boundary conditions when simulating the rarefaction effects at hypersonic flows. Similar CFD results are also reported in Ref. [25, 26].

Fig. 13 and 14 show the pressure coefficient and Stanton number along the surface with the three meshes using no-slip boundary conditions. The results computed by the medium mesh (CFD2) coincide with that of the fine mesh (CFD3), which indicates that the mesh convergence is reached.

### c. Computations with slip boundary conditions

Fig. 15 shows the  $Kn_{GLL}$  contours of HCTF which

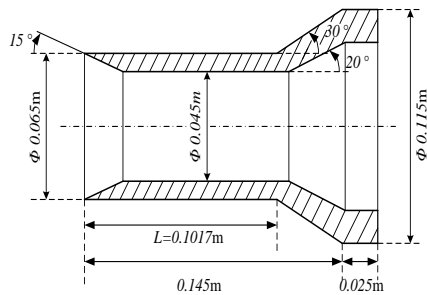


Fig. 9. HCTF configuration

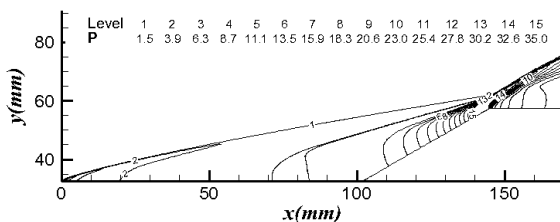


Fig. 11. Pressure contours for HCTF

is computed from the density field of CFD3. The gray regions and black regions correspond to  $Kn_{GLL} > 0.05$  are observed in the leading edge, in the shock region and in a thin boundary layer along the surface. It means the continuum assumption breakdown there. Therefore, the slip boundary conditions are necessary in current simulations.

Fig. 16 presents the distribution of the slip velocity  $u_s$  along the surface by using the Maxwell boundary conditions. The  $|U|$  in Fig. 16 refers to velocity magnitude along the wall, the negative parts mean the recirculation region where  $u < 0$ . The slip velocity appears larger than the gas velocity of the DSMC result. This disagreement is due to the inaccurate physical model within the Knudsen layer. After calculating from a simple relation<sup>[26]</sup>  $u_g = 0.696u_s$ , derived from the linearized Boltzmann equation, the gas velocity is in good agreement with the DSMC result. The wall quantities using different boundary conditions are shown in Fig. 17 and 18. It can be seen that the results of slip boundary conditions agree better than that of no-slip boundary conditions. With slip boundary conditions, the separation region is smaller than that with no-slip boundary conditions, which is also shown in the Table 2. The “CFD-S” cases refer to those simulated using the slip boundary conditions.

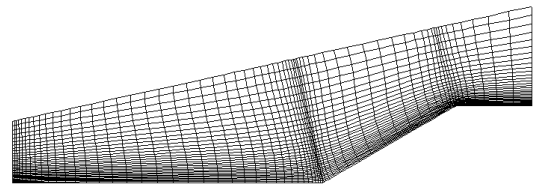


Fig. 10. The fine mesh for the HCTF (skip=8)

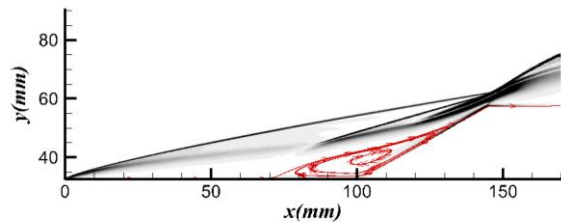


Fig. 12. Numerical schlieren picture and streamlines at the corner

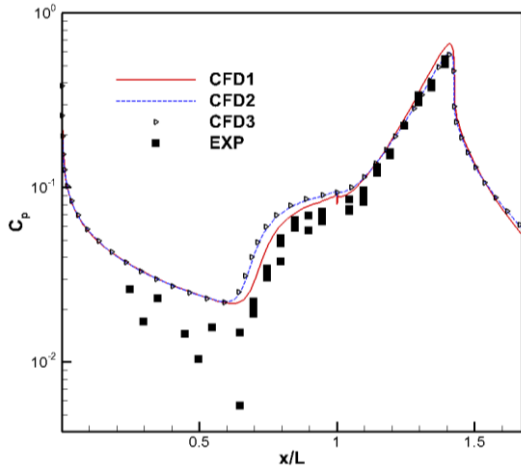


Fig. 13. Pressure coefficient along the surface using different meshes

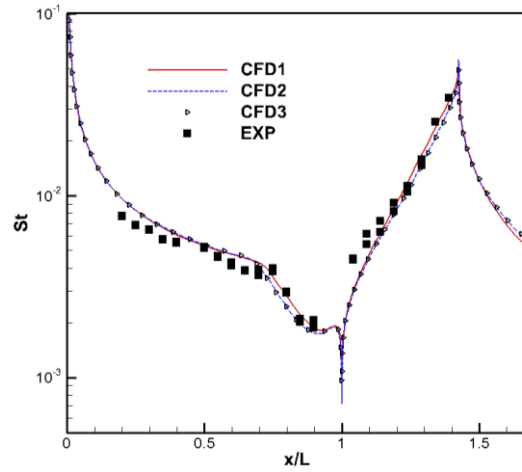


Fig. 14. Stanton number along the surface using different meshes

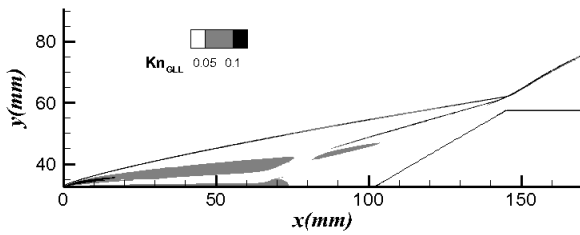


Fig. 15.  $Kn_{GLL}$  field for HCTF

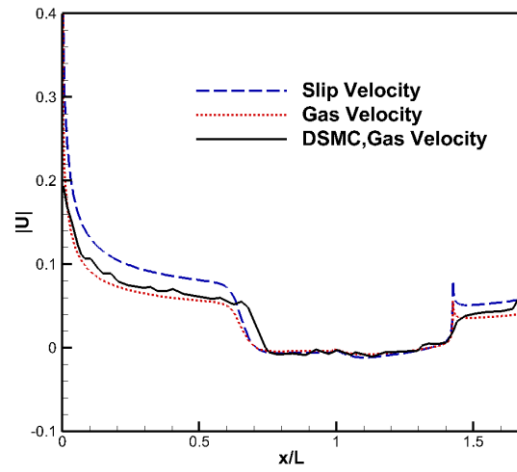


Fig. 16. Slip velocity along the surface for HCTF

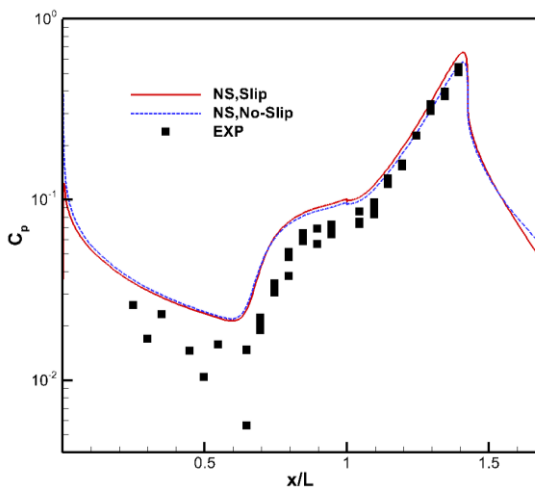


Fig. 17. Pressure coefficient along the surface using different boundary conditions

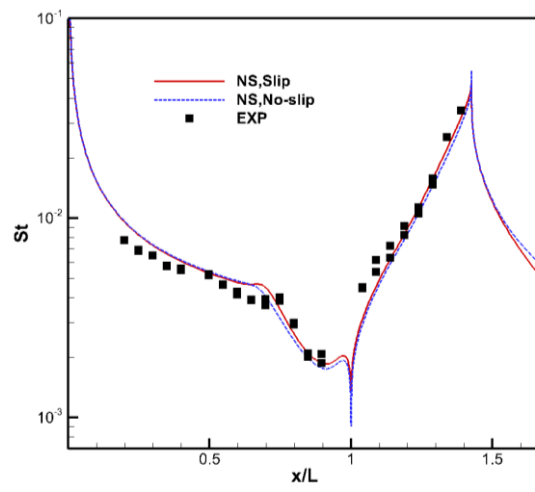


Fig. 18. Stanton number along the surface using different boundary conditions

**Table 2 Separation and reattachment point locations for different cases**

Case	Mesh	Wall BCs	$X_S/L$	$X_R/L$
CFD1	128×128	No-slip	0.745	1.336
CFD2	256×256	No-slip	0.718	1.345
CFD3	512×256	No-slip	0.718	1.345
CFD1-S	128×128	Slip	0.765	1.329
CFD2-S	256×256	Slip	0.727	1.341
CFD3-S	512×256	Slip	0.726	1.342
DSMC [25]	-	-	0.77	1.32
Experiment [25]	-	-	0.76±0.01	1.34±0.015

### 3.2 Sharp double cone

Hypersonic flow of nitrogen around a 25°/55° sharp cone (SDC) is calculated here. The configuration and the sample mesh are shown in Fig. 19. The inflow conditions corresponds to RUN 7 experimental conditions in the Calspan-University at Buffalo Research Center (CUBRC) 48-inch shock tunnel.

The freestream conditions are  $T_\infty = 42.6K, T_w = 297K, \rho_\infty = 1.75 \times 10^{-4} kg/m^3, Re_\infty = 1.375 \times 10^5 / m, Ma_\infty = 15.6$ . A laminar flow is ensured in this condition. The Sutherland law is used for modeling the dynamic viscosity, where the related parameters are the same as the HCEF case. The setup of boundary conditions is also the same as those in the HCEF case. The experimental data and DSMC results are from Ref. [29, 30].

#### a. Flow structures

The complex interaction structures are presented in Fig. 20. The oblique shock formed from the first cone combines with the separation shock, forming a merged shock which impinges on the bow shock caused by the second cone. Meanwhile the supersonic jet is formed behind the shocks. The pressure contours and streamlines at the corner are also shown in this Fig. 20. The shock waves and the vortex structures are clearly to be seen. The separation vortex is generated due to the viscous boundary layer and the geometry deflection.

#### b. Mesh convergence

Four different meshes are conducted to validate the numerical results of the study. The number of mesh points are 133×64, 266×128, 512×256 and 738×384 in the streamwise and the normal directions, respectively. Table 3 presents the separation and reattachment point locations with different meshes. The recirculation region length increases with the mesh refinement, which is similar to the phenomenon in the HCTF case.

Fig. 21 and 22 show the pressure and the heat transfer along the surface with the aforementioned four meshes using the no-slip boundary conditions. It can be seen that the physical quantities are mesh convergent.

#### c. Computations with slip boundary conditions

To show the local extent of rarefaction,  $Kn_{GLL}$  contours is presented in Fig. 23. The continuum breakdown occurs in the shock region, the thin boundary layer along the surface of first cone, and the second corner. Both the no-slip boundary condition and the Maxwell slip boundary conditions are used in this case.

Fig. 24 provides the slip velocity distributions along the surface. By the modification of the formula  $u_g = 0.696u_s$ , the NS result agrees well with the DSMC result<sup>[30]</sup>. As shown in Fig. 25 and 26, the pressure and heat transfer distributions along the surface calculated with the fine mesh (738×384) are presented. The pressure agrees well with the experimental data, and the heat transfer is slightly lower than the experiment. The divergence is about 15% before the separation point and 20% after the reattachment point. Compared with no-slip boundary conditions, the slip ones generate some

different results in the leading edge and the first cone where the  $Kn_{GLL}$  is greater than 0.05. Regarding the separation zone, the size by slip boundary conditions is

slightly smaller than that by the no-slip boundary conditions results. The results indicate that it has few rarefied effects in this case.

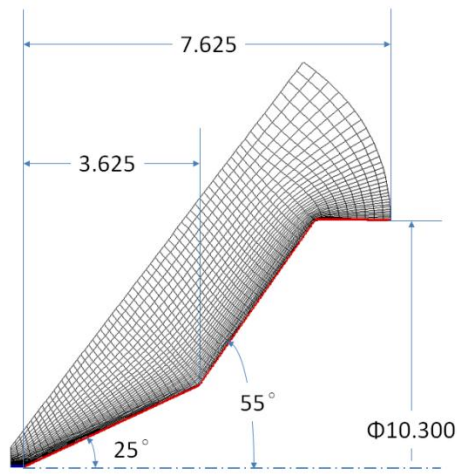


Fig. 19. Computational mesh for the 25°/55°SDC (dimensions in inch)

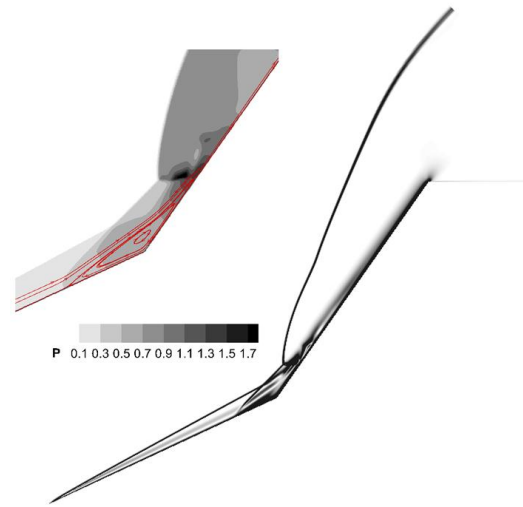


Fig. 20. Numerical schlieren picture, pressure contours and streamlines at the corner

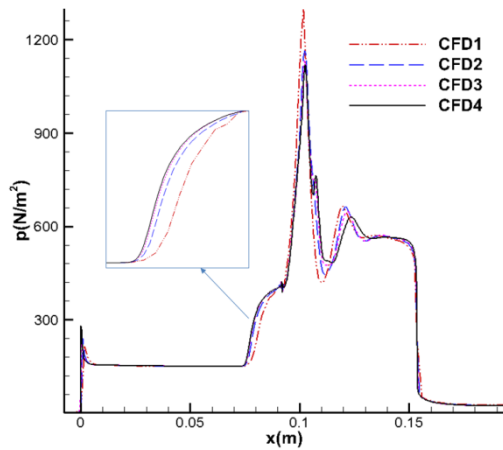


Fig. 21. Pressure along the surface using different meshes

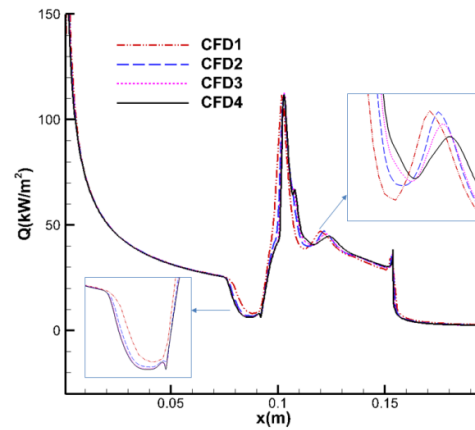


Fig. 22. Heat transfer along the surface using different meshes

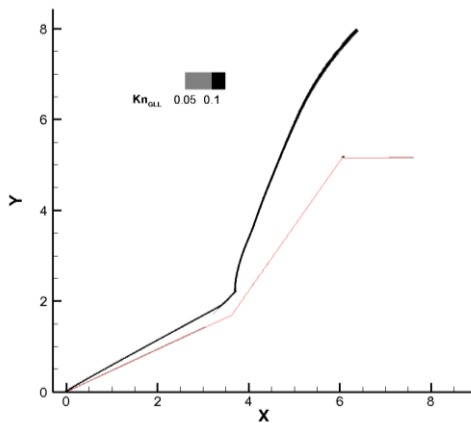


Fig. 23.  $Kn_{GLL}$  field for 25°/55°SDC

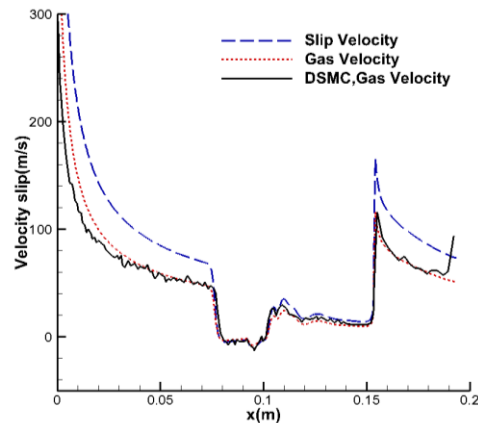


Fig. 24. Slip velocity along the surface for SDC

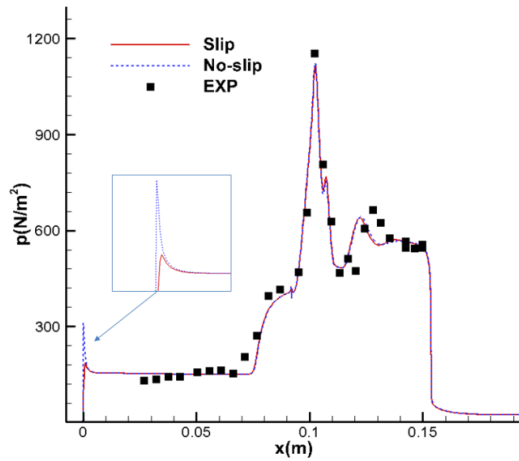


Fig. 25. Pressure along the surface using different boundary conditions

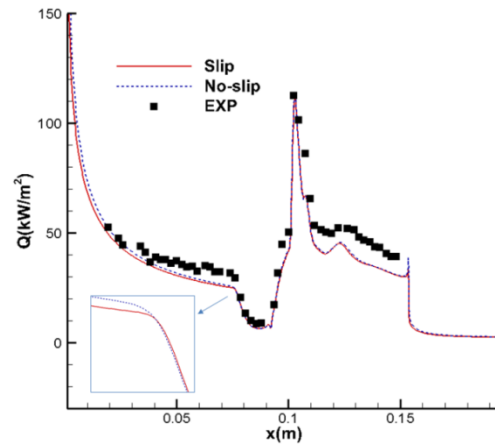


Fig. 26. Heat transfer along the surface using different boundary conditions

Table 3 Separation and reattachment point locations for different meshes

Case	133×64 (CFD1)	266×128 (CFD2)	512×256 (CFD3)	738×384 (CFD4)	738×384 (Slip)	DSMC[27]
$X_S$ (mm)	81.2	79.0	78.1	78.0	78.1	80.4
$X_R$ (mm)	99.4	101.0	101.6	101.7	101.7	100.8

## 4 Conclusions

Hypersonic shock wave/boundary layer interactions with different boundary conditions is simulated and discussed by the WENO-OS3 scheme in this paper.

Firstly, the WENO-OS3 scheme is presented, which is optimized by adding a downwind candidate stencil to the WENO3 scheme. A free parameter  $n_{3rd}$  is introduced to represent the numerical dissipation of the scheme. For the nonlinear part, the algorithm with a variation of the power is presented, which aims at improving the performance of the scheme further. The Shu-Osher problem shows that the resolution of the WENO-OS3 scheme is better than the second-order NND and WENO3 scheme. The flat plate shock wave / boundary layer interaction problem and the sharp double cone problem indicate that the WENO-OS3 scheme is better than the NND scheme but worse than the WENO5 scheme on flow structure description and heat transfer prediction. Secondly, the implementation of the Maxwell slip boundary conditions is given, which is demonstrates correctly by the flat plate case. The circular cylinder

cases show that it is acceptable to simulate the hypersonic flows within the slip regime by using NS equations with the Maxwell slip boundary conditions. Finally, hypersonic flows around the hollow cylinder truncated flare and the 25° sharp double cone are studied. Discussions are made on the characteristics of the hypersonic shock wave/boundary layer interactions with and without the consideration of the slip effect. With the slip boundary conditions, the separation region at the corner is smaller and its prediction is more accurate than that with no-slip boundary conditions.

In conclusion, the present study reveals the good performance of the WENO-OS3 scheme in hypersonic shock wave/boundary layer interactions. The scheme will be used for more complicated simulations and engineering applications in the future.

## Acknowledgements

This research has been supported by National Key Basic Research and Development Program (2014CB744100).

## Appendix

When characteristic variables are used in the WENO-OS3 scheme, a corresponding factor  $\Phi_2$  will be introduced in the *rescale* function. Because the threshold values ( $p_{11}$  and  $p_{1u}$ ) are obtained by the one dimensional code where left matrix  $L_{ref}$  is used, they are not available when other forms of characteristic matrix are used.

Therefore, a diagonal matrix  $\Phi_2$  must be used for *rescaling* when they are applied to the three dimensional (3D) code whose left matrix is  $L$ . If left matrix  $L$  in the 3D code are the same as the  $L_{ref}$ , the  $\Phi_2$  turns to be an identity matrix. In this paper,  $L$  and  $L_{ref}$  are different, and they are defined as follows:

$$L_{ref} = \begin{bmatrix} \frac{1}{2a^2}(\phi^2 + a\bar{\theta}) & -\frac{1}{2a^2}[(\gamma-1)u + \bar{k}_x a] & -\frac{1}{2a^2}[(\gamma-1)v + \bar{k}_y a] & -\frac{1}{2a^2}[(\gamma-1)w + \bar{k}_z a] & \frac{1}{2a^2}(\gamma-1) \\ \bar{k}_x \left(1 - \frac{\phi^2}{a^2}\right) + \bar{k}_z \frac{v}{a} - \bar{k}_y \frac{w}{a} & \frac{\bar{k}_x}{a^2}(\gamma-1)u & \frac{\bar{k}_x}{a^2}(\gamma-1)v - \frac{\bar{k}_z}{a} & \frac{\bar{k}_x}{a^2}(\gamma-1)w + \frac{\bar{k}_y}{a} & -\frac{\bar{k}_x}{a^2}(\gamma-1) \\ \bar{k}_y \left(1 - \frac{\phi^2}{a^2}\right) + \bar{k}_x \frac{w}{a} - \bar{k}_z \frac{u}{a} & \frac{\bar{k}_y}{a^2}(\gamma-1)u + \frac{\bar{k}_z}{a} & \frac{\bar{k}_y}{a^2}(\gamma-1)v & \frac{\bar{k}_y}{a^2}(\gamma-1)w - \frac{\bar{k}_x}{a} & -\frac{\bar{k}_y}{a^2}(\gamma-1) \\ \bar{k}_z \left(1 - \frac{\phi^2}{a^2}\right) + \bar{k}_y \frac{u}{a} - \bar{k}_x \frac{v}{a} & \frac{\bar{k}_z}{a^2}(\gamma-1)u - \frac{\bar{k}_y}{a} & \frac{\bar{k}_z}{a^2}(\gamma-1)v + \frac{\bar{k}_x}{a} & \frac{\bar{k}_z}{a^2}(\gamma-1)w & -\frac{\bar{k}_z}{a^2}(\gamma-1) \\ \frac{1}{2a^2}(\phi^2 - a\bar{\theta}) & -\frac{1}{2a^2}[(\gamma-1)u - \bar{k}_x a] & -\frac{1}{2a^2}[(\gamma-1)v - \bar{k}_y a] & -\frac{1}{2a^2}[(\gamma-1)w - \bar{k}_z a] & \frac{1}{2a^2}(\gamma-1) \end{bmatrix},$$

$$L = \begin{bmatrix} \frac{1}{\sqrt{2}a}(\phi^2 + a\bar{\theta}) & -\frac{1}{\sqrt{2}a}[(\gamma-1)u + \bar{k}_x a] & -\frac{1}{\sqrt{2}a}[(\gamma-1)v + \bar{k}_y a] & -\frac{1}{\sqrt{2}a}[(\gamma-1)w + \bar{k}_z a] & \frac{1}{\sqrt{2}a}(\gamma-1) \\ \frac{\bar{k}_x}{a}(a^2 - \phi^2) + \bar{k}_z v - \bar{k}_y w & \frac{\bar{k}_x}{a}(\gamma-1)u & \frac{\bar{k}_x}{a}(\gamma-1)v - \bar{k}_z & \frac{\bar{k}_x}{a}(\gamma-1)w + \bar{k}_y & -\frac{\bar{k}_x}{a}(\gamma-1) \\ \frac{\bar{k}_y}{a}(a^2 - \phi^2) + \bar{k}_x w - \bar{k}_z u & \frac{\bar{k}_y}{a}(\gamma-1)u + \bar{k}_z & \frac{\bar{k}_y}{a}(\gamma-1)v & \frac{\bar{k}_y}{a}(\gamma-1)w - \bar{k}_x & -\frac{\bar{k}_y}{a}(\gamma-1) \\ \frac{\bar{k}_z}{a}(a^2 - \phi^2) + \bar{k}_y u - \bar{k}_x v & \frac{\bar{k}_z}{a}(\gamma-1)u - \bar{k}_y & \frac{\bar{k}_z}{a}(\gamma-1)v + \bar{k}_x & \frac{\bar{k}_z}{a}(\gamma-1)w & -\frac{\bar{k}_z}{a}(\gamma-1) \\ \frac{1}{\sqrt{2}a}(\phi^2 - a\bar{\theta}) & -\frac{1}{\sqrt{2}a}[(\gamma-1)u - \bar{k}_x a] & -\frac{1}{\sqrt{2}a}[(\gamma-1)v - \bar{k}_y a] & -\frac{1}{\sqrt{2}a}[(\gamma-1)w - \bar{k}_z a] & \frac{1}{\sqrt{2}a}(\gamma-1) \end{bmatrix},$$

where  $a$  is the sound speed,  $\phi^2 = \frac{1}{2}(\gamma-1)(u^2 + v^2 + w^2)$ ,  $\bar{\theta} = \frac{k_x u + k_y v + k_z w}{\sqrt{k_x^2 + k_y^2 + k_z^2}}$ ,  $\bar{k}_x = \frac{k_x}{\sqrt{k_x^2 + k_y^2 + k_z^2}}$ , the definitions

of  $\bar{k}_y$  and  $\bar{k}_z$  are similar to that of  $\bar{k}_x$ , and  $k$  refers to  $\xi$ ,  $\eta$ ,  $\zeta$  when it is discretized in *computational coordinates* respectively. Then the  $\Phi_2$  is obtained, i.e.

$$\Phi_2 = L_{ref}^{-1} L = \text{diag}\left(1/(\sqrt{2}a), 1/a, 1/a, 1/a, 1/(\sqrt{2}a)\right).$$

## References:

[1] HOLDEN M S, WADHAMS T P, MACLEAN M. A review of experimental studies with the double cone and hollow cylinder/flare configurations in the LENS hypervelocity tunnels and comparisons with Navier-Stokes and DSMC computations [C]. AIAA

paper 2010-1281.

[2] LOFTHOUSE A J. Nonequilibrium hypersonic aerothermodynamics using the direct simulation Monte Carlo and Navier-Stokes models [D]. Ph. D. Dissertation, the University of Michigan, 2008.

[3] MAXWELL J C. On stresses in rarefied gases arising from inequalities of temperature [J]. Philosophical

Transactions of the Royal Society.1879, 170: 231-256.

[4]M. von SMOLUCHOWSKI, Über wärmeleitung in verdünnten gasen [J]. Annalen der Physik und Chemie, 1898, 64: 101-130.

[5]GÖKÇEN T, MACCORMACK R W, CHAPMAN D. R. Computational fluid dynamics near the continuum limit [C]. AIAA paper 87-1115.

[6]GÖKÇEN T, MACCORMACK R W. Nonequilibrium effects for hypersonic transitional flows using continuum approach [C].AIAA Paper 1989-0461.

[7]LOCKERBY D A, REESE J M, GALLIS M A. Capturing the Knudsen layer in continuum-fluid models of nonequilibrium gas flows [J]. AIAA Journal, 2005, 43(6): 1391-1393.

[8]DEISSLER R. An analysis of second-order slip flow and temperature-jump boundary conditions for rarefied gases [J]. International Journal of Heat and Mass Transfer, 1965, 7: 681-694.

[9]BESKOD A, KARNIADAKIS G. Rarefaction and compressibility effects in gas micro flows [J]. Journal of Fluids Engineering, 1996, 11: 448-456.

[10]YILDIZ B, Gokturk T. An extension to the first order slip boundary conditions to be used in early transition regime [C]. AIAA paper 2002-2779.

[11]LOCKERBY D A, REESE J M, EMERSON D R, et al. The velocity boundary condition at solid walls in rarefied gas calculations [J]. Physical Review E: Statistical, Nonlinear, and Soft Matter Physics, 2004, 70 (1): 017303.

[12]NAM T P, LE C W, JASON M R, et al. Langmuir-Maxwell and Langmuir-Smoluchowski boundary conditions for thermal gas flow simulations in hypersonic aerodynamics [J]. International Journal of Heat and Mass Transfer, 2012, 55: 5032-5043.

[13]ZHANG H X, ZHUANG F G. NND schemes and their applications to numerical simulation of two- and three- dimensional flows [J]. Advances in Applied Mechanics, 1991, 29: 193-256.

[14]LIU X, OSHER S, CHAN T. Weighted essentially non-oscillatory schemes [J]. Journal of Computational Physics, 1994, 115: 200-212.

[15]JIANG G S, SHU C W. Efficient implementation of weighted ENO schemes [J]. Journal of Computational Physics, 1996, 126(1): 202-228.

[16]SHEN Y Q, ZHA G C, HUERTA M A. Simulation of hypersonic shock wave/boundary layer interaction

using high order WENO scheme [C]. AIAA paper 2010-1047.

[17]LIU X, DENG X G. Application of high-order accurate algorithm to hypersonic viscous flows for calculating heat transfer distributions [C]. AIAA paper 2007-691.

[18]OLIVEIRA M L, XIE P, SU J Z, et al. Modified weighted compact scheme for shock-boundary layer interaction and double cone [C]. AIAA paper 2008-755.

[19]LI Q, SUN D, ZHENG Y K, et al. On a class of center-typed third order difference scheme orienting to engineering utilizations [J]. ACTA Aerodynamica Sinica, 2013, 31(4): 466-472. (in Chinese)

[20]BOYD I D, CHEN G, CANDLER G V. Predicting failure of the continuum fluid equations in transitional hypersonic flows [J]. Physics of Fluids, 1995, 7(1): 210-219.

[21]SHU C W, OSHER S. Efficient implementation of essentially non-oscillatory shock-capturing schemes [J]. Journal of Computational Physics, 1989, 83: 32-78.

[22]MACCORMACK R W. A numerical method for solving the equations of compressible viscous flow [J]. AIAA Journal, 1982, 20(9): 1275-1281.

[23]GNOFFO P. CFD validation studies for hypersonic flow prediction [C]. AIAA paper 2001-1025.

[24]BECKER M. Flat plate flow field and surface measurements from merged layer into transition regime [C]. Proceedings of the seventh International Symposium on Rarefied Gas Dynamics, 1969, 515-528.

[25]GORCHAKOVA N, KUZNETSOV L, YARYGIN V. Progress in hypersonic studies using electron-beam-excited X-Ray detection [J]. AIAA Journal. 2002, 40(4): 593-598.

[26]MARKELOV G N, KUDRYAVTSEV A N, IVANOV M S. Continuum and kinetic simulation of shock wave/laminar boundary layer interaction in hypersonic flows [C]. AIAA paper 1999-3527.

[27]LI Q B, FU S. Application of gas-kinetic scheme with kinetic boundary conditions in hypersonic flow [J]. AIAA Journal. 2005, 43(10): 2170-2176.

[28]MORTAZAVI M, KNIGHT D. Shock wave boundary layer interaction in a hypersonic laminar flow on a hollow cylinder flare [C]. AIAA paper 2016-0351.

[29]HOLDEN M S, WADHAMS T P, CANDLER G V, et al. Measurements in regions of low density laminar shock wave/boundary layer interaction in hypervelocity

flows and comparison with Navier–Stokes predictions [C]. AIAA paper 2003-1131.

[30] JAMES N M, BIRD G A. Direct simulation Monte Carlo simulations of hypersonic flows with shock interactions [J]. AIAA Journal, 2005, 43(12): 2565-2573.

**Li Chen** received the B.Eng. degree in School of Aerospace Engineering from Beijing Institute of Technology, Beijing, China, in 2011 and M.E. degree in Fluid Mechanics from China Aerodynamics Research and Development Center (CARD), Mianyang, China, in 2014. In July 2011, he joined the State Key Laboratory of Aerodynamics, Mianyang, China.

**Guo Qilong** received the B.Eng. degree in Thermal

Science and Energy Engineering from University of Science and Technology of China, Hefei, China, in 2010 and M.E. degree in Fluid Mechanics from CARD, Mianyang, China in 2013. In July 2010, he joined the State Key Laboratory of Aerodynamics, Mianyang, China.

Prof. **Li Qin** received B.Eng. degree in School of Aerospace Engineering from National University of Defense Technology, Changsha, China, in 1991. He currently works in the State Key Laboratory of Aerodynamics, Mianyang, China.

Prof. **Zhang Hanxin** is an academician of Chinese Science Academy. He currently works in National CFD Laboratory of Aerodynamics, NUAA, Beijing, China.